Journal of Materials Chemistry A

Inorganic Salt Reinforced Zn2+-conducting Solid-state Electrolyte for Ultra-stable Zn Metal Battery

Journal:	*Journal of Materials Chemistry A*
Manuscript ID	TA-ART-07-2019-007218.R1
Article Type:	Paper
Date Submitted by the Author:	30-Aug-2019
Complete List of Authors:	Han, Qi; Shanghai Institute of Ceramics Chinese Academy of Sciences chi, xiaowei; Shanghai Institute of Ceramics Chinese Academy of Sciences Liu, Yunzhao; Shanghai Institute of Ceramics Chinese Academy of Sciences Wang, Liang ; Beijing Institute of Technology Du, Yuexiu; Shanghai Institute of Ceramics Chinese Academy of Sciences Ren, Yang; Argonne National Laboratory, Liu, Yu; Shanghai Institute of Ceramics Chinese Academy of Sciences,

Inorganic Salt Reinforced Zn^{2+}-conducting Solid-state Electrolyte for Ultra-stable Zn Metal Battery

Qi Han[a,b], Xiaowei Chi[a,*],Yunzhao Liu[a,b], Liang Wang[c], Yuexiu Du[a,b], Yang Ren[d], Yu Liu[a,*]

[a] Shanghai Institute of Ceramics, Chinese Academy of Sciences, Shanghai 200050, P.R. China

[b] University of Chinese Academy of Sciences, Beijing 100049, P.R. China

[c] School of Materials Science and Engineering, Beijing Institute of Technology, Beijing 100081, P.R. China

[d] X-ray Science Division, Argonne National Laboratory, Argonne IL 60439, USA

Corresponding Authors:

*Email: *xwchi@mail.sic.ac.cn; yuliu@mail.sic.ac.cn*

Abstract: The rapid development of flexible and wearable electronics calls for advanced batteries with high safety, long cycling stability, and low cost. Aqueous Zn metal batteries (ZMBs) are one of the most promising candidates. The main challenges are the water-induced parasitic reactions (corrosion and passivation) and dendrites-driven battery failure in traditional liquid electrolyte. Developing new electrolyte systems is critical to overcoming these issues. Herein, an ultrastrong self-standing gelatin-based solid-state electrolyte (GSE) formed by strong hydrophobic interaction between gelatin molecule chains is firstly introduced for stable solid-state ZMBs. The GSEs prepared by a facile soaking strategy contain much less free water compared to conventional electrolyte systems and exhibit the highest fracture tensile strength of 2.78 MPa among the reported self-standing single-component solid-state electrolytes for ZMBs, which effectively inhibit the corrosion/passivation reaction and enable the Zn/Zn symmetric cells to stably cycle at hitherto the highest current density of 5 mA cm^{-2} with record cumulative plating/stripping capacity. Meanwhile, the solid-state Zn/MnO_2 full cell can deliver a high reversible specific capacity of 285 mAh g^{-1}, superior cycling stability (90% capacity retention/500 cycles), and excellent safety under extremely working circumstances. The impressive performance sheds light on the design and applications of robust solid-state electrolytes for ZMBs.

1. Introduction

Flexible and wearable electronics, “Holy Grail” of the next-generation consumer electronic products, have sprung up recently. However, their development poses great challenges in the inner energy storage/conversion devices, which should not only provide reliable power but also guarantee superior safety and flexibility. Nowadays, much progress in the energy storage/conversion devices based on super-capacitors and lithium-ion batteries have been achieved[1-5]. The former possesses high power density and excellent cycle performance, however, suffers from unsatisfied energy density. In contrast, the latter with high energy density has dominated the portable electronic market in the past two decades. Unfortunately, in the wearable devices that require extremely high safety, the applications of the lithium-ion batteries are largely restricted due to the intrinsic safety hazards derived from the leakage and flammability of non-aqueous liquid electrolytes. Quite the opposite, aqueous solid-state electrolytes that are nonflammable and nonflowable are, therefore, ideal electrolyte candidates for wearable devices.

As to the electrodes, metals are more promising since they usually have excellent ductility to meet the requirements for flexibility. Zn metal as the anode has recently been proposed in aqueous batteries due to its attractive advantages of the low redox potential of –0.78 V (versus SHE), high theoretical gravimetric and volumetric specific capacities of 820 mAh g^{-1} and 5855 mAh cm^{-3}, respectively, low cost, and environmental friendliness[6-9]. So far, some solid-state electrolytes based on poly(vinyl alcohol)[10-12], poly(acryl amide)[13-16], fumed silica[17], xanthan gum[18], and poly(ethylene oxide)-poly(propylene oxide)-poly(ethylene oxide)[19] have been developed for Zn metal batteries (ZMBs). These solid-state electrolytes offer remarkable flexibility for the solid-state ZMBs, however, they only allow the cycling of Zn metal at low current densities (< 2 mA cm^{-2}), which is unfavorable for the power density of the full cells and the electronics. The fundamental reason is the high content of free water (> 70%) in the solid-state electrolytes. Free water not only causes surface corrosion and passivation of Zn metal but also dramatically decreases the intrinsic mechanical strength of the corresponding polymers. As a consequence, it is critical to reducing the water content for improving the mechanical properties of the solid-state electrolytes. In our previous work, we prepared gelatin-based solid-state electrolyte (GSE) through fast cooling technique[20]. As shown in Scheme 1a and 1b, the fast cooling promotes the randomly dispersed gelatin molecules to locally aggregate into helical segments by hydrogen bonding interaction. In detail, at the temperatures above the gelation temperature (T_g), gelatin coils randomly disperse in aqueous solution. Upon cooling, the random gelatin molecules spontaneously form linkages through hydrogen bonds and the chains undergo a conformational disorder–order transition to generate triple-helix segments[21]. Further, the helices can coil together and finally transform into the GSE. The as-prepared GSE shows compressive strength of 100 kPa. In addition to the unique thermal reversibility, GSE was found to tolerate the high amount of inorganic salts. Furthermore, intriguingly, the introduction of inorganic salts results in dehydration of the GSE[22]. By harnessing the unique salt-reinforced effect of GSE, in this work, the as-prepared GSE was further treated in concentrated inorganic salt solutions that lead to strong hydrophobic interactions between gelatin molecular chains and enhanced chain bundling within the gel network (Scheme 1b and 1c). This facile yet powerful approach was proved to increase the mechanical strength of GSE by 1~2 orders of magnitude, to 2.78 MPa, which is the highest among the single-component and self-standing solid-state Zn^{2+}-conducting electrolyte systems. Although it is slightly lower than those of the composite electrolyte systems (e.g. gelatin-*g*-PAM[22]), which generally require complicated fabrication processes and increase the cost, the robust GSE we newly developed was obtained by facile soaking treatment without any other second support and more advantageous in scalable device fabrication.

Furthermore, unlike those of the previously reported solid-state electrolytes with high water content, our newly prepared salt-reinforced GSEs contain much less water (~45% vs 78.16% for pristine GSE) and thus exhibits higher stability for both Zn metal anode and MnO_2 cathode. In particular, the current density and cycle life of the Zn metal anode are remarkably improved. The salt-reinforced GSE enables the Zn metal to stably cycle at a record current density of 5 mA cm^{-2} for 400 cycles without short-circuiting. As a result, the cumulative plating/stripping capacity is as high as 2000 mAh cm^{-2}, within our knowledge, which is the highest among the solid-state ZMBs, and even comparable to liquid ZMBs with surface-modified Zn metal. Furthermore, the new strategy provides substantially robust solid-state electrolyte and extremely safe Zn/MnO_2 full battery that can resist harsh working conditions including being cut, bent, hammered, punctured, and even soaked in water without any packaging. To elucidate the excellent performance, synchrotron XRD, SEM, TEM, and HADDF-STEM of Zn and MnO_2 electrodes during cycling were implemented.

2. Experimental section

2.1 Preparation of the salt reinforced gelatin-based solid-state electrolytes (GSEs)

Gelatin powers (4 g, AR, Aladdin) were dissolved into 40 g aqueous solution composed of $ZnSO_4$ (1 M, AR, Aladdin) and $MnSO_4$ (0.1 M, AR, Aladdin) under stirring at 60 °C. The obtained gelatin solution was injected into a home-made mold of 150 mm × 150 mm × 0.5 mm. The solution was cooled rapidly down to 1 °C to form the pristine GSE. Subsequently, these GSEs were immersed into $ZnSO_4$/$MnSO_4$ mixed solution at various concentrations of $ZnSO_4$ (1.0, 1.5, 2.0, 2.5, 3.0, and 3.5 M) and constant $MnSO_4$ concentration of 0.1 M at room temperature for 48 h to prepare the reinforced GSEs.

2.2 Synthesis of MnO_2/CNT composite cathode material

The carboxyl-functionalized MWCNT (1 g, ~95wt%, Suzhou Tanfeng Technology Co., Ltd.) powders were homogeneously dispersed in deionized water (120 mL) under vigorous stirring and ultrasonication for 3 h. Then, $Mn(CH_3COO)_2 \cdot 4H_2O$ (2.94 g, AR, Aladdin) was dissolved into above dispersion, which was then added drop-wise into a $KMnO_4$ aqueous solution (1.27 g/80 mL, AR, Aladdin). The mixed solution after stirring for 3 h was transferred to a Teflon-lined autoclave and heated at 120 °C for 12 h. After cooling, the obtained dark brown precipitate was washed several times by deionized water and vacuum-dried at room temperature for 8 h to finally obtain the MnO_2/CNT composite powders.

2.3 Fabrication of the electrodes and assembly of solid-state ZMBs

MnO_2/CNT composite, acetylene black, and PVDF powders were mixed with a weight ratio of 7:2:1 in N-methyl-2-pyrrolidone (NMP) solvent to obtain a cathode slurry, which was then coated with a doctor blade on stainless-steel foil and vacuum-dried at 70 °C for 12 h. The mass loading of MnO_2 active material is about 1.0−1.5 mg cm^{-2}. The MnO_2/CNT as the cathode, GSE-2.5 as the electrolyte and separator, and Zn foil as the anode were sandwiched in pouch cells (2×3.5 cm^2) with PE plastic films under vacuum of −0.1 MPa for 1 min without extra external force to assemble solid-state ZMBs. During the following electrochemical tests, no pressure was applied on the cells.

2.4 Material characterization

The high-energy synchrotron X-ray diffraction (XRD) technique was performed at 11-ID-C beamline of Advanced Photon Source, Argonne National Laboratory, USA. A monochromatic X-ray beam with a size of 0.2×0.2 mm² and a wavelength of 0.1173 Å was used. A PerkinElmer α-Si flat-panel large-area detector with a quadratic pixel size of 200×200 μm^2 was placed behind the specimen to collect the two-dimensional (2D) diffraction patterns during loading. 2D diffraction patterns and the subsequent XRD analysis were all conducted by using the software GSAS II. The field emission scanning electron microscope (FESEM, Hitachi S-4800) was employed to determine the morphologies of the surface of MnO_2/CNT cathodes at different discharging/charging states and Zn anodes in cycled Zn/GSE-0 or GSE-2.5/Zn symmetric cells. The cathode samples for FESEM tests were pre-sputtered with gold. The morphologies and microstructures of the MnO_2/CNT composite powders and the corresponding composite cathodes discharged to 0.9 V were observed by transmission electron microscope (FEI Titan3 G2 60-300 TEM) equipped with an aberration-corrector for the imaging lenses for high resolution TEM (HRTEM), a high-angle annular dark-field (HAADF) detector for STEM imaging, and an energy dispersive X-ray (EDX) detector for composition mapping. The thermal property of GSEs was measured by differential scanning calorimeter (DSC, NETZSCH STA 449) from room temperature to 80 °C at a heating rate of 5 °C min^{-1} under N_2 atmosphere. Thermal gravimetric (TG) tests of MnO_2/CNT composite and CNT were conducted on the thermal gravimetric analysor (TGA, NETZSCH STA 409 PC) from room temperature to 800 °C at a heating rate of 10 °C min^{-1} under air atmosphere. The tensile tests of dumbbell GSE samples (12.5 mm in width and 20 mm in length) were performed with the universal testing system (Instron 5566) at a tensile speed of 10 mm min^{-1}.

The rates of swelling or shrinking (φ) of the GSE before and after soaking in inorganic salt solution at various concentrations of $ZnSO_4$ were calculated by Equation

4:

$$\varphi = {(W_w - W_o)}/{W_o} \times 100\% \quad (4)$$

Where W_o and W_w represent the weight of the GSE before and after soaking. The samples were weighed at intervals after the removal of the excess surface solution with Kimwipes paper.

The water content (W_{H_2O}), gelatin content (W_{gel}), and salt content (W_{salt}) of the GSEs were calculated using Equations (5), (6), and (7).

$$W_{H_2O} {(W_w - W_d)}/{W_w} \times 100\% \quad (5)$$

$$W_{gel} = {(W_g \times c_g)}/{W_w} \times 100\% \quad (6)$$

$$W_{salt} = {(W_d - W_g \times c_g)}/{W_w} \times 100\% \quad (7)$$

Where W_w and W_d are the weights of the GSEs before and after drying at 60 °C in an oven for 48 h, respectively, W_g is the weight of the gelatin gel before soaking into salt solution, and c_g is the mass concentration of the gelatin solution.

2.5 Electrochemical Measurement

The conductivity of the GSEs was measured using electrochemical impedance spectroscopy technique. The test was conducted by sandwiching the electrolytes between two stainless steel (SS) foils over a frequency range of 1 MHz to 100 mHz with an amplitude of 10 mV on the electrochemical station (AUTOLAB PGSTAT 302N) under open-circuit voltage (OCV) condition at 25 °C. The ionic conductivity σ (S cm^{-1}) was calculated according to Equation 8:

$$\sigma = {d}/{(SR_b)} \quad (8)$$

Where R_b(Ω) is the bulk resistance (intercept at Z' axis), and *S* is the contact area between the electrolyte and SS foils (2 × 2 cm^2), *d* represents the thickness of the GSE. For the GSE-0, GSE-1.5, GSE-2.0, GSE-2.5, GSE-3.0, GSE-3.5 the *d* are 0.500 mm, 0.448 mm, 0.275 mm, 0.235 mm, 0.201 mm, and 0.191 mm, respectively.

Zn/GSE-x/SS asymmetric cells were assembled to conduct linear sweep voltammetry test and cyclic voltammetry test at different scanning rates on the electrochemical station (AUTOLAB) at 25 °C. Galvanostatic discharging-charging and cycling tests were performed on LANHE battery tester in the voltage range of 0.9 V−1.85 V at 25 °C.

2.6 Destructive tests

The planar thin film batteries (2 × 7 cm^2) were firstly discharge-charged, and then used to power the electric watch under various extreme condition (being cut, immersed in water, bent, hammered, and drilled). And in order to study the flexibility of the inorganic salt reinforced-GSEs, the charging-discharging performance of the planar batteries were monitored under being bent or hammered for 20 times.

3. Results and discussion

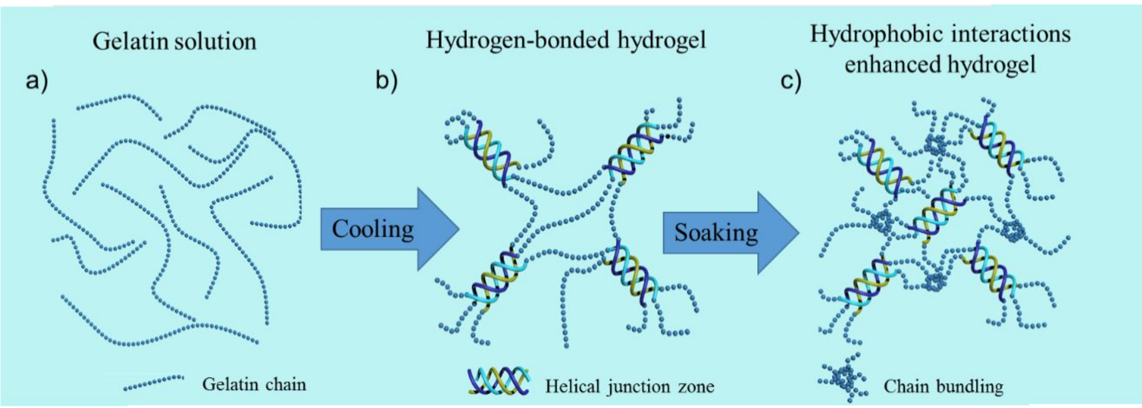

Scheme 1. The schematic illustration of molecular conformation of (a) gelatin solution, (b) gelatin solid-state electrolyte (GSE-0), and (c) salt-reinforced GSE-x (x=1.0, 1.5, 2.0, 2.5, 3.0, and 3.5) after soaking the GSE-0 in $ZnSO_4$/$MnSO_4$ solution.

The pristine GSE (GSE-0) was prepared by the casting method[23]. As mentioned above, to reduce the water content and reinforce the GSE's mechanical strength, the pristine GSE-0 was treated with $ZnSO_4$/$MnSO_4$ salt solution at various concentrations of $ZnSO_4$ (1.0, 1.5, 2.0, 2.5, 3.0, and 3.5 M. 3.5 M $ZnSO_4$ is oversaturated). The treated GSEs were abbreviated as GSE-x, where x represents the molar concentration of $ZnSO_4$. Due to the synergistic hydrogen bonding interaction and hydrophobic interaction between the gelatin chains (Scheme 1), inorganic salt solutions show a significant effect on the physical properties of GSEs.

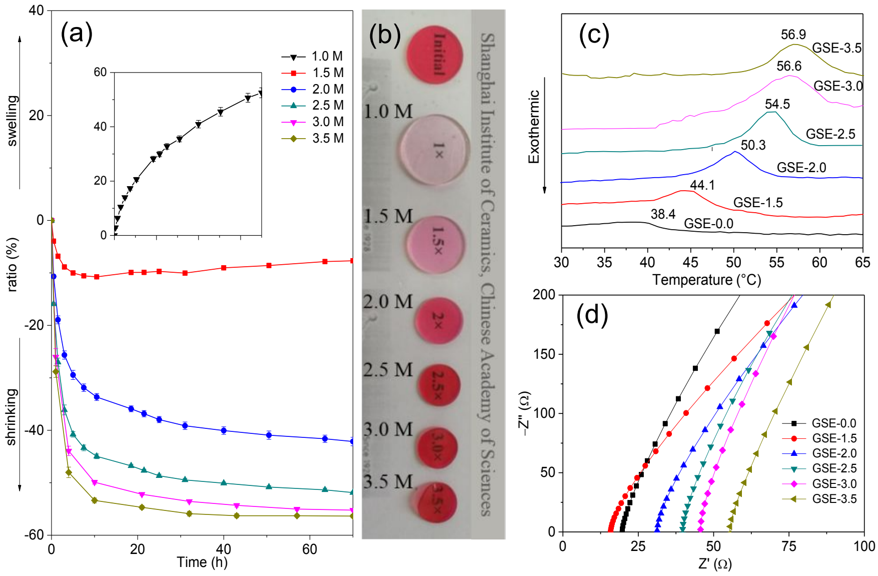

Figure 1. Characterization of GSE-x (x=1.0, 1.5, 2.0, 2.5, 3.0, and 3.5). (a) Swelling and shrinking ratios; (b) Optical images; (c) DSC curves; (d) EIS spectra.

After immersion in those inorganic salt solutions, the GSEs exhibited different swelling/shrinking behaviors (Figure 1b). As seen in Figure 1a, GSE-1.0 showed 52% swelling; in stark contrast, when the salt concentration increased beyond 1.5 M, the GSEs began to shrink due to the elevated osmotic pressure in the surrounding environment and showed a maximum shrinking ratio of −56% at the concentration of 3.5 M. The swelling and shrinking behaviors are mainly related to the water absorption and dehydration of GSEs. From the component content of GSEs in Table S1 (Supporting Information), the higher concentration of the soak solution corresponds to the lower water content, on the contrary, higher salt content in the GSEs. As the salt concentration increased to 2.5 M, the water content dramatically decreased to 45.35%. Further increase of the salt solution to 3.5 M leads to little change. The significant decrease of water content in the GSE-x (x > 1.5) is, on one hand, beneficial for enhancing the thermal stability, mechanical strength of GSEs, and safety of the GSE-based batteries under harsh conditions; on the other, favorable for improving the cycling stability since the free water molecules are the root of the undesired instability of GSEs towards Zn metal anode.

In order to evaluate the thermal stability of the GSEs before and after soaking treatment, DSC curves of GSE-x were tested and shown in Figure 1c. The pristine GSE-

0 shows the lowest transformation temperature of 38.4 °C due to the weak physical hydrogen bonding crosslinking. In comparison, owing to the stronger hydrophobic interaction induced by the inorganic salt, the stable temperature of GSE-x (x > 2.0) is elevated to above 50 °C. The electrochemical impedance spectroscopy (EIS) and linear sweep voltammetry (LSV) were then performed to determine the ionic conductivities and oxidation stability of GSE-x. As seen in Figure 1d, with the increase of x from 1.5 to 3.5, the conductivity of GSE-x gradually decreases since the content of free water that can facilitate the ionic transport of the GSE-x decreases. The oxidation current in LSV curves (Figure S1) of GSE-x increases observably above 2.0 V, which is related to the decomposition reaction of water. Meanwhile, the weak current at 1.8 V is probably ascribed to oxidation of Mn^{2+} from the electrolyte[24].

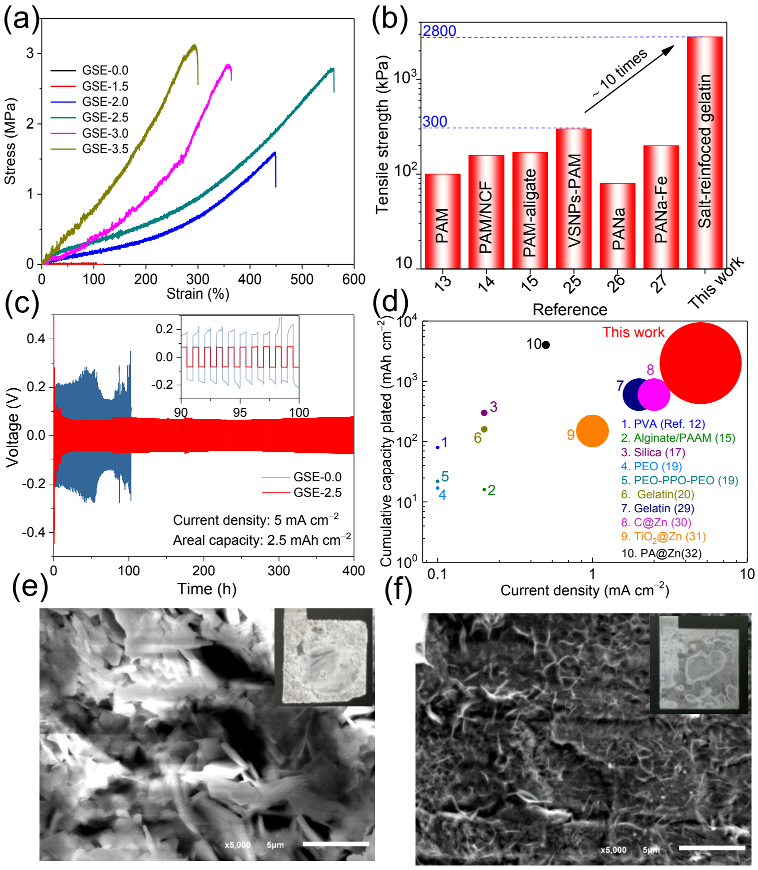

Figure 2. Mechanical properties and symmetric cells performance of GSE-x (x=1.0, 1.5, 2.0, 2.5, 3.0, and 3.5). (a) Stress-strain curves of the GSE-x; (b) Comparison of tensile strength of GSE-2.5 with those of reported self-standing solid-state electrolytes for aqueous Zn-based batteries; (c) Galvanostatic cycling of Zn/GSE-0/Zn and Zn/GSE-2.5/Zn solid-state symmetric cells at current density of 5 mA cm^{-2}; (d) Comparison on cycling performance of Zn/Zn symmetric cells using GSE-2.5 and other

reported solid-state electrolytes as well as liquid electrolytes and modified Zn metal anode. The current density, areal plating/stripping capacity of the Zn anode per cycle (size of each circle), and cumulative capacity were summarized in this plot; (e, f) Optical and SEM images of Zn electrodes after cycling (400 cyles at current density of 5 mA cm^{-2}) in the Zn/Zn symmetric cells using GSE-0 and GSE-2.5 as solid-state electrolytes, respectively. Scale bar: 5 μm.

It is remarkable the GSE-x after immersion in salt solution exhibit superior mechanical strength (Figure S2, Movie S1, Supporting Information), the stress-strain curves in Figure 2a detail the correlation between solution concentration and tensile strength of the GSE-x. As the salt solution concentration increases, significant improvement in the tensile strength is observed, which is attributed to the enhanced hydrophobic interaction and the lessened water content. The GSE-2.5 delivers a fracture tensile strength of 2.78 MPa at a strain of 560%, while GSE-0 was too fragile to clamp for the tensile tests. Taking consideration of all the properties (Figure S3, Supporting Information), GSE-2.5 possessing excellent mechanical strength, thermal stability, and decent ionic conductivity simultaneously was, therefore, chosen for the following studies. Furthermore, compared with the reported self-standing solid-state electrolytes for aqueous batteries (Figure 2b), the GSE-2.5 presents the highest tensile strength[25-27]. The exceptional mechanical performance will provide the GSE adequate strength to resist Zn dendrites. Zn/GSE/Zn symmetric cells were then assembled to confirm that. As presented in Figure 2d, the Zn/Zn symmetric cell with GSE-0 shows larger polarization and especially suffers from dendrite short-circuiting after 100 h. In stark contrast, due to the less free water in GSE-2.5 and Zn/GSE-2.5/Zn symmetric cell exhibits very flat voltage profile and stable cycling at a current density as high as 5 mA cm^{-2} for over 400 cycles. It needs to mention that the GSE-0 and GSE-2.5 have different thickness of 0.500 mm and 0.235 mm, respectively. To exclude the thickness effect, we further compared the GSE-2.5 with different thickness. As shown in Figure S4, the thinner GSE-2.5-0.235 mm shows comparable stability to the thicker GSE-2.5-0.513 mm, indicating the little influence of thickness difference of GSE-0 and GSE-2.5 on the symmetric cells. For metal batteries, the areal current density, areal plating/stripping capacity per cycle, and the total cumulative capacity of the metal anodes are the most important three parameters since they are closely related to the power density, energy density, cycling performance of the metal batteries, respectively[28]. Therefore, we further compared these parameters of the Zn metal anodes in GSE-2.5-based symmetric cell in this work with those of recent publications in other solid-state or liquid electrolyte systems. From Figure 2d, it is apparent that those previously reported Zn metal anodes were cycled at small current densities and with low cumulative capacities. In contrast, our ultrastrong GSE-2.5 enables the Zn metal anode to present superior cycling performance, including the areal current density and the total cumulative capacity, both of which are to the best of our knowledge the record among solid-state Zn metal batteries[29-32]. The SEM image (Figure 2e) and XRD result (Figure S5, Supporting Information) of Zn electrode after 400 cycles in symmetrical cells based on pristine GSE shows obvious change of the surface morphology (Zn dendrites) and side reaction products of zinc hydroxide sulfate hydrate. In comparison, the GSE-2.5 (Figure 2f) are more stable towards Zn metal, indicating its great potential for the Zn metal-based full batteries.

Due to the unique tunnel structure that can facilitate the insertion/desertion process of Zn^{2+} cations, α-MnO_2 was chosen as the cathode active material to pair with Zn metal anode. Carbon nanotubes (CNTs) were incorporated into α-MnO_2 to enhance the electronic conductivity of MnO_2. The α-MnO_2/ CNT composite cathode material was obtained by the hydrothermal method, exhibiting uniform morphology of nanorod with fine crystallinity (Figure S6, Supporting Information). Furthermore, the CNTs with an external diameter of 10–30 nm (SEM image in Figure S7, Supporting Information) evenly distributed with α-MnO_2 nanorods (TEM image and HADDF-STEM images in Figure S8a and Figure S9, Supporting Information). The high-resolution transmission electron microscopy (HRTEM) image further shows that the MnO_2 is α-phase that has the an inter-planar spacing of 0.685 nm for the (110) plane (Figure S8b, Supporting Information). From the thermal gravimetric (TG) results (Figure S10, Supporting Information), the total carbon content in α-MnO_2/CNT composite is determined to be 7.79%. The α-MnO_2/CNT was then applied as the cathode to assemble the solid-state ZMB.

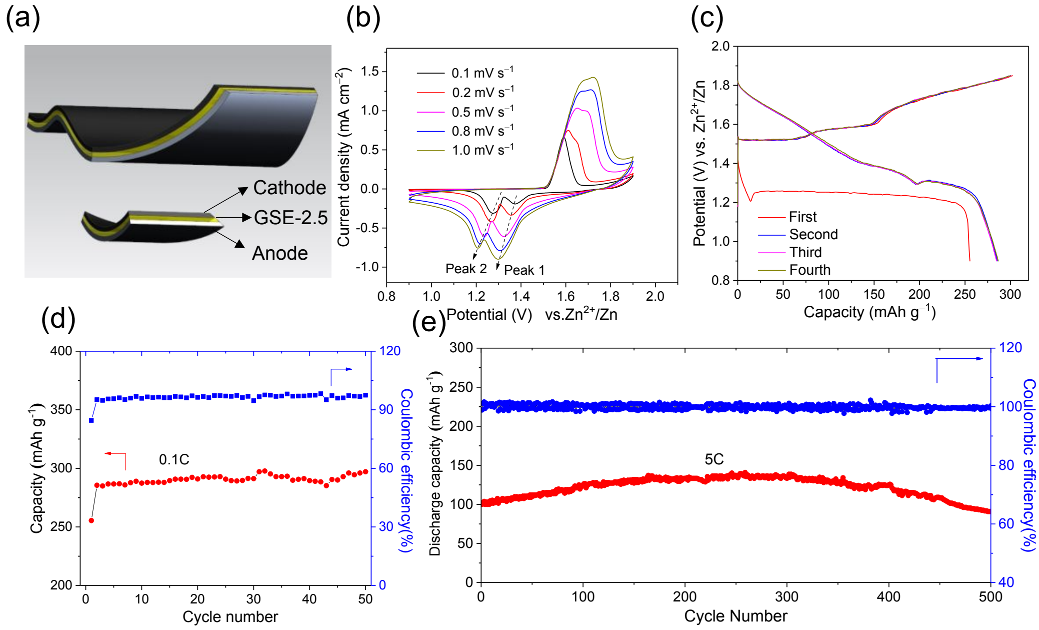

Figure 3. Electrochemical performance of solid-state Zn/GSE-2.5/MnO_2 batteries: (a) Schematic illustration of the structure of the solid-state ZIB; (b) CV curves at various scanning rates; (c) Charge-discharge voltage profiles of the initial four cycles at 0.1C; (d) Cycle performance at 0.1C; (e) Cycle performance at 5C. (1C=308 mA g^{-1})

Figure 3a shows the scheme of the flexible solid-state ZMB that is fabricated by sandwiching α-MnO_2/CNT cathode, GSE-2.5 solid-state electrolyte, and Zn metal anode in an open-air environment, which is facile and efficient.The cyclic voltammetry (CV) curves of solid-state ZMBs within 0.9 V−1.9 V at different scanning rates were collected and shown in Figure 3b, Two obvious cathodic peaks located at 1.35 V (Peak 1) and 1.25 V (Peak 2) can be defined. With the scanning rate increasing from 0.1 mV s^{-1} to 1 mV s^{-1}, the peak current of Peak 1 significantly rises and becomes the dominant peak; however, the Peak 2 shows less change of peak current, indicating different reaction kinetics are associated with these two cathodic peaks. The reaction mechanism will be systamtically elucidated in the following studies. Figure 3c presents the initial four charge/discharge voltage profiles of the ZMB based on GSE-2.5 at 0.1C. It is notable that the first discharging profile was significantly different from the following ones. It may be attributed to the irreversible structural transformation of the α-MnO_2 cathode during the first discharge process[33, 34].. However, the reversible process takes place in the subsequent cycles. Furthermore, as mentioned above, the much lower amount of free water in the GSE-2.5 than GSE-0, which alleviates the side reactions between water and electrodes, and higher mechanical strength of GSE-2.5, which suppresses the dendrite growth of Zn anode and the dissolution of MnO_2 active material, endow the GSE-2.5-based ZMB with excellent cycling stability of 100%/50 cycles and 90%/500 cycles at 0.1C and 5C (Figure 3d and 3e), respectively. It is noteworthy of pointing out that the ascending discharge capacity in intial cycles is due to the activation process of MnO_2 in the solid-state electrolyte. Since the Zn^{2+}/H^+ co-insertion processes (to be confirmed in the Figure 4) happen in the discharge process of MnO_2, on one hand, the H^+ ions are from the dissociation of water molecules that requires to gradually diffuse from the solid-state electrolyte into the MnO_2 electrodes, resulting in the capacity increase; on the other hand, according to the literature[14, 22, 35], the strong electrostatic interaction between divalent Zn^{2+} ions and crystal structures also results in an initial activation, especially cycling at high rate. Furthermore, compared with other GSE-based solid-state ZMBs (e.g. Zn/GSE-0/MnO_2 and Zn/GSE-3.5/MnO_2, Figure S11 and S12), the Zn/GSE-2.5/MnO_2 ZMB shows comparable rate capability to the former using more conductive GSE-0 and higher discharge capacity than the latter using more robust GSE-3.5.

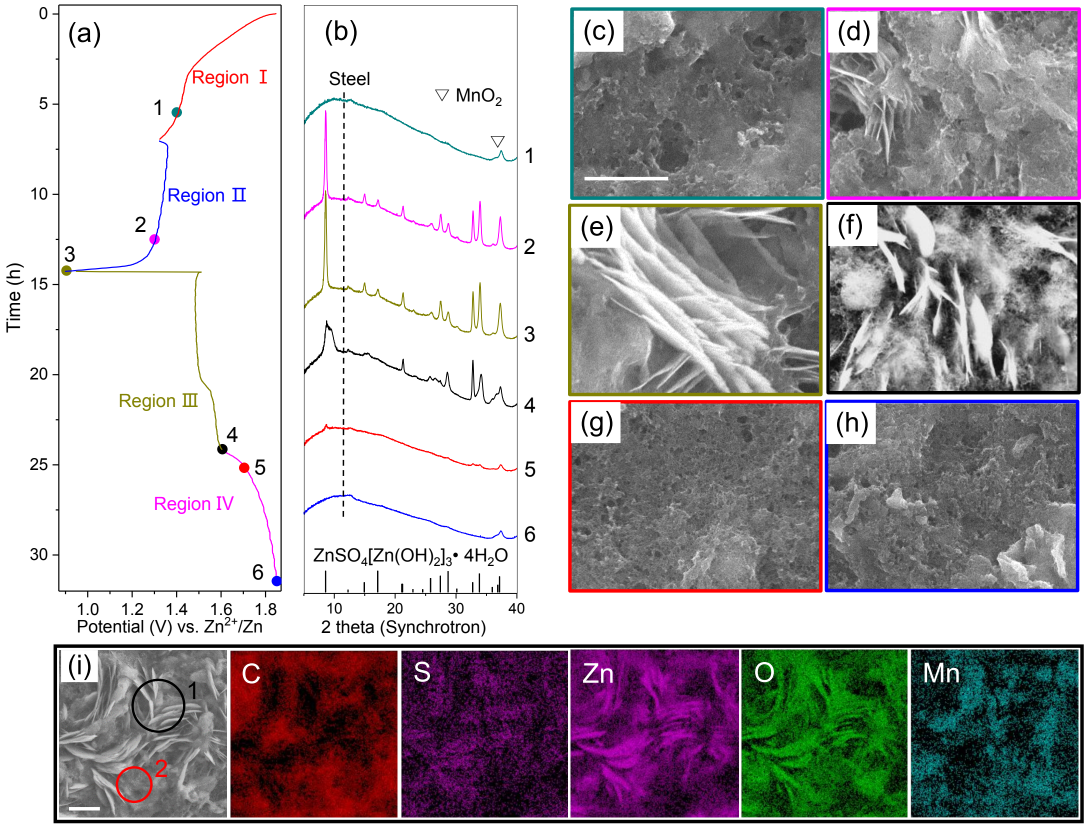

Figure 4. Structure and morphology evolution of MnO_2 cathode in the solid-state

Zn/GSE-2.5/MnO_2 ZIB during cycling. (a) Charge-discharge voltage profiles of the 2nd cycle; (b) Ex-situ synchrotron XRD patterns of MnO_2 cathodes at different discharging/charging states; (c-h) The corresponding SEM images of states 1 to 6, respectively. Scale bar is 10 μm; (i) SEM and EDS mapping images of state 3 (fully discharged state) in 4(a). Scale bar is 10 μm. SEM images show two kinds of morphologies for the discharged products: one is flake-like (circle 1); the other is particle-shape (circle 2).

The reaction mechanism of MnO_2 in salt-reinforced GSEs was further investigated for a better knowledge of the reversible and stable charge/discharge process of solid-state Zn/GSE-2.5/MnO_2 ZMB. *Ex-situ* synchrotron XRD patterns of α-MnO_2/CNT at different discharging/charging states of the second cycle at 30 mA g^{-1} (Figure 4a) were shown in Figure 4b. In the first discharge region (Region I, red color), only one diffraction peak at 37.3° indexed to MnO_2 (JCPDS 44–0141) was observed (XRD pattern 1). However, some diffraction peaks arise at the second discharge plateau (Region II, blue color), including three strong peaks at 8.5°, 32.7°, 33.9° and three relatively weaker peaks at 21.2°, 27.5° and 28.7° (XRD patterns 2 and 3), which are the characteristic peaks of $ZnSO_4(Zn(OH)_2)_3{\cdot}4H_2O$ (JCPDS 44–0673). It indicates that $ZnSO_4(Zn(OH)_2)_3{\cdot}4H_2O$ is the discharged products of MnO_2 in solid-state ZMB. During the subsequent charge process (Region III and IV), the previously arisen peaks weaken (XRD patterns 4 and 5), and finally disappear (XRD pattern 6), suggesting the discharged products are reversible. To further identify the reversible behavior of MnO_2 in solid-state ZMBs, SEM images are further analyzed to unravel the morphologic transformation of the MnO_2 cathode. It is clear to observe the highly reversible change of morphology from Fig. 4c-h. A large number of flake-like and small amount of particle-shape discharged products emerge in discharging Region II and vanish after charging Region III, which is well consistent with the reversible evolution of crystalline structure in XRD patterns. First, for the flake-like products, EDS analysis (Figure 4a, S13, Supporting Information) shows that the flake-like product is abundant in Zn, O, and S elements, but scarce of Mn element, which verifies that the flakes are zinc hydroxide sulfate hydrate. The formation of zinc hydroxide sulfate hydrate is attributed to the insertion of H^+ (Equation 1). With the consumption of H^+ in the region I, the OH^-

anions decomposed from water react with $ZnSO_4$ and H_2O in the electrolyte in Equation 2 to form flake-like zinc hydroxide sulfate in region II[34, 36].

$$MnO_2 + H^+ + e^- \leftrightarrow MnOOH \tag{1}$$

$$\frac{1}{6}Zn^{2+} + OH^- + \frac{1}{6}ZnSO_4 + \frac{4}{6}H_2O \leftrightarrow \frac{1}{6}ZnSO_4[Zn(OH)_2]_3 \cdot 4H_2O \tag{2}$$

Additionally, as to the particle-shape discharged products, HAADF-STEM image of sample 3 and corresponding EDX mapping result (Supporting Information, Figure S14) indicates the formation of the $ZnMn_2O_4$ after fully discharging of MnO_2, reflecting the existence of Zn^{2+} insertion process (Equation 3). Therefore, for MnO_2 in GSE-based solid-state ZMB, the reaction mechanism is consequent H^+ and Zn^{2+} insertion . This mechanism is same as that of liquid battery[32, 33].

$$Zn^{2+} + 2MnO_2 + 2e^- \leftrightarrow ZnMn_2O_4 \tag{3}$$

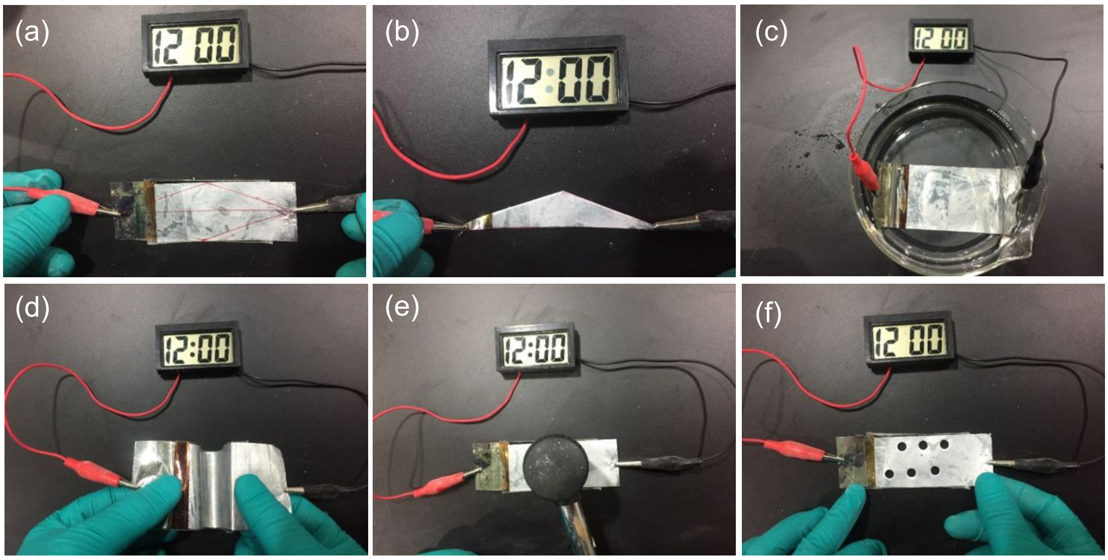

Figure 5. Destructive tests of solid-state Zn/GSE-2.5/MnO_2 ZMBs: (a), (b) Cutting test; (c) Soaking test; (d) Bending test; (e) Hammering test; (f) Drilling test.

For flexible devices application, durability and safety are of great importance for the batteries. To investigate the stability of our newly developed solid-state Zn/GSE-2.5/MnO_2 battery, a series of extreme working conditions and even some destructive tests were conducted. It is remarkable that the solid-state Zn/GSE-2.5/MnO_2 batteries are capable of powering an electronic watch even after being cut for several times (Figure 5a-b, Movie S2, Supporting Information). Impressively, due to the ultrastrong mechanical properties of salt-reinforced GSE-2.5 solid-state electrolyte, the batteries without any sealing component can consistently function well under being immersed in water (Figure 5c, Movie S3, Supporting Information), bent (Figure 5d, Movie S4, Supporting Information), hammered (Figure 5e, Movie S5, Supporting Information), and drilled (Figure 5f, Movie S6, Supporting Information). Moreover, as shown in Figure S16, no obvious capacity loss (rentions are 95.3% and 95%, respectively) was observed after the batteries were bent for 200 times or hammered for 100 times, demonstrating superb safety performance and encouraging future application of solid-state Zn/GSE-2.5/MnO_2 batteries in flexible devices.

4. Conclusion

To conclude, by taking advantage of the inorganic salt-reinforced effect for gelatin, a strong and durable self-standing gelatin-based solid-state electrolyte (GSE-2.5) with a record high fracture tensile strength of 2.78 MPa among all the self-standing single-component solid-state electrolytes for ZMBs was obtained for solid-state Zn metal batteries without complicated, toxic chemical modification or the addition of reinforcing fillers. The solid-state Zn/GSE-2.5/MnO_2 battery exhibits high reversible specific capacities of 285 mAh g^{-1} at 0.1C and excellent cycling stability with capacity retention of 90%/500 cycles at 5C benefiting from the reversible consequent H^+ and Zn^{2+} co-insertion/desertion mechanism of MnO_2 in GSE-2.5 solid-state electrolyte. Moreover, the solid-state battery exhibits superior safety and excellent flexibility under extreme conditions, such as being cut, immersed in water, bent, hammered and drilled. This study not only makes clear the reaction mechanism of solid-state Zn/MnO_2 battery but also provides a facile fabrication of strong solid-state electrolyte with great potential in flexible and wearable energy storage devices.

Acknowledgements

This work was financially supported by the Ministry of Science and Technology of Shanghai (No. 16XD1424600). The use of Advanced Photon Source at Argonne National Laboratory was supported by U.S. Department of Energy [No.DE-AC02-06CH11357]. The authors thank Dr. Gang Wan for analyzing the synchrotron X-ray diffraction (XRD) patterns and Xinghao Lin for drawing the schematic diagram.

References

1. Z. Weng, Y. Su, D. W. Wang, F. Li, J. H. Du and H. M. Cheng, *Adv. Energy Mater.*, 2011, **1**, 917-922.
2. X. H. Lu, M. H. Yu, G. M. Wang, Y. X. Tong and Y. Li, *Energy Environ. Sci.*, 2014, **7**, 2160-2181.
3. M. S. Balogun, H. Yang, Y. Luo, W. T. Qiu, Y. C. Huang, Z. Q. Liu and Y. X. Tong, *Energy & Environmental Science*, 2018, **11**, 1859-1869.
4. H. P. Wu, S. A. Shevlin, Q. H. Meng, W. Guo, Y. N. Meng, K. Lu, Z. X. Wei and Z. X. Guo, *Advanced Materials*, 2014, **26**, 3338-+.
5. G. Qian, B. Zhu, X. Liao, H. Zhai, A. Srinivasan, N. J. Fritz, Q. Cheng, M. Ning, B. Qie, Y. Li, S. Yuan, J. Zhu, X. Chen and Y. Yang, *Adv. Mater.*, 2018, **30**, e1704947.
6. M. Song, H. Tan, D. L. Chao and H. J. Fan, *Adv. Funct. Mater.*, 2018, **28**.
7. G. Fang, J. Zhou, A. Pan and S. Liang, *ACS Energy Lett.*, 2018, **3**, 2480-2501.
8. Y. Li, J. Fu, C. Zhong, T. Wu, Z. Chen, W. Hu, K. Amine and J. Lu, *Adv. Energy Mater.*, 2019, **9**, 1802605.
9. H. Li, L. Ma, C. Han, Z. Wang, Z. Liu, Z. Tang and C. Zhi, *Nano Energy*, 2019, **62**, 550-587.
10. Y. Zeng, X. Zhang, Y. Meng, M. Yu, J. Yi, Y. Wu, X. Lu and Y. Tong, *Adv. Mater.*, 2017, **29**, 1700274.
11. B. He, Q. Zhang, L. Li, J. Sun, P. Man, Z. Zhou, Q. Li, J. Guo, L. Xie, C. Li, X. Wang, J. Zhao, T. Zhang and Y. Yao, *J. Mater. Chem. A*, 2018, **6**, 14594-14601.
12. S. Huang, F. Wan, S. Bi, J. Zhu, Z. Niu and J. Chen, *Angew. Chem. Int. Ed. Engl.*, 2019, **58**, 4313-4317.
13. Z. Wang, F. Mo, L. Ma, Q. Yang, G. Liang, Z. Liu, H. Li, N. Li, H. Zhang and C. Zhi, *ACS Appl. Mater. Interfaces*, 2018, **10**, 44527-44534.
14. D. Wang, H. Li, Z. Liu, Z. Tang, G. Liang, F. Mo, Q. Yang, L. Ma and C. Zhi, *Small*, 2018, **14**, 1803978.
15. Z. Liu, D. Wang, Z. Tang, G. Liang, Q. Yang, H. Li, L. Ma, F. Mo and C. Zhi, *Energy Storage Mater.*, 2019, DOI: https://doi.org/10.1016/j.ensm.2019.03.007.
16. H. Li, Q. Yang, F. Mo, G. Liang, Z. Liu, Z. Tang, L. Ma, J. Liu, Z. Shi and C. Zhi, *Energy Storage Mater.*, 2019, **19**, 94-101.
17. J. Huang, X. Chi, Q. Han, Y. Liu, Y. Du, J. Yang and Y. Liu, *Journal of The Electrochemical Society*, 2019, **166**, A1211-A1216.
18. S. Zhang, N. Yu, S. Zeng, S. Zhou, M. Chen, J. Di and Q. Li, *J. Mater. Chem. A*, 2018, **6**, 12237-12243.
19. J. Zhao, K. K. Sonigara, J. Li, J. Zhang, B. Chen, J. Zhang, S. S. Soni, X. Zhou, G. Cui and L. Chen,

Angew. Chem. Int. Ed. Engl., 2017, **56**, 7871-7875.
20. Q. Han, X. Chi, S. Zhang, Y. Liu, B. Zhou, J. Yang and Y. Liu, *J. Mater. Chem. A*, 2018, **6**, 23046-23054.
21. A. Bigi, S. Panzavolta and K. Rubini, *Biomaterials*, 2004, **25**, 5675-5680.
22. H. Li, C. Han, Y. Huang, Y. Huang, M. Zhu, Z. Pei, Q. Xue, Z. Wang, Z. Liu, Z. Tang, Y. Wang, F. Kang, B. Li and C. Zhi, *Energy Environ. Sci.*, 2018, **11**, 941-951.
23. Y. Guo, X. Zhou, Q. Tang, H. Bao, G. Wang and P. Saha, *J. Mater. Chem. A*, 2016, **4**, 8769-8776.
24. N. Zhang, F. Cheng, J. Liu, L. Wang, X. Long, X. Liu, F. Li and J. Chen, *Nat. Commun.*, 2017, **8**.
25. Y. Huang, M. Zhong, F. Shi, X. Liu, Z. Tang, Y. Wang, Y. Huang, H. Hou, X. Xie and C. Zhi, *Angew. Chem. Int. Ed. Engl.*, 2017, **56**, 9141-9145.
26. J. Liu, M. M. Hu, J. Q. Wang, N. Y. Nie, Y. Y. Wang, Y. K. Wang, J. H. Zhang and Y. Huang, *Nano Energy*, 2019, **58**, 338-346.
27. Y. Huang, J. Liu, J. Wang, M. Hu, F. Mo, G. Liang and C. Zhi, *Angew Chem Int Ed Engl*, 2018, DOI: 10.1002/anie.201805618.
28. C. Yang, H. Xie, W. Ping, K. Fu, B. Liu, J. Rao, J. Dai, C. Wang, G. Pastel and L. Hu, *Adv. Mater.*, 2019, **31**, e1804815.
29. J. Zhao, H. Ren, Q. Liang, D. Yuan, S. Xi, C. Wu, W. Manalastas, J. Ma, W. Fang, Y. Zheng, C.-F. Du, M. Srinivasan and Q. Yan, *Nano Energy*, 2019, **62**, 94-102.
30. W. Li, K. Wang, M. Zhou, H. Zhan, S. Cheng and K. Jiang, *ACS Appl. Mater. Interfaces*, 2018, **10**, 22059-22066.
31. K. Zhao, C. Wang, Y. Yu, M. Yan, Q. Wei, P. He, Y. Dong, Z. Zhang, X. Wang and L. Mai, *Adv. Mater. Interfaces*, 2018, **5**, 1800848.
32. Z. Zhao, J. Zhao, Z. Hu, J. Li, J. Li, Y. Zhang, C. Wang and G. Cui, *Energy Environ. Sci.*, 2019, **12**, 1938-1949.
33. W. Sun, F. Wang, S. Hou, C. Yang, X. Fan, Z. Ma, T. Gao, F. Han, R. Hu, M. Zhu and C. Wang, *J. Am. Chem. Soc.*, 2017, **139**, 9775-9778.
34. J. Huang, Z. Wang, M. Hou, X. Dong, Y. Liu, Y. Wang and Y. Xia, *Nat. Commun.*, 2018, **9**, 2906.
35. M. Liu, Q. Zhao, H. Liu, J. Yang, X. Chen, L. Yang, Y. Cui, W. Huang, W. Zhao, A. Song, Y. Wang, S. Ding, Y. Song, G. Qian, H. Chen and F. Pan, *Nano Energy*, 2019, **64**, 103942.
36. H. Pan, Y. Shao, P. Yan, Y. Cheng, K. S. Han, Z. Nie, C. Wang, J. Yang, X. Li, P. Bhattacharya, K. T. Mueller and J. Liu, *Nat. Energy*, 2016, **1**, 16039.